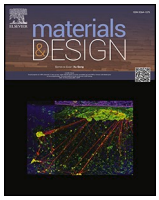
Materials & Design 257 (2025) 114434



Contents lists available at ScienceDirect

Materials & Design

journal homepage: www.elsevier.com/locate/matdes





Utilizing machine learning to predict tensile ductility and yield strength of CoNiV-based multi-principal elements alloys☆

H.C. Ozdemir [a,b], D. Canadinc [a], O. El Atwani [c], J. Valdez [b], B. Lovato [b], C. Mathews [b], J. Wanni [b], J. Cooley [d], S.J. Fensin [b,*]

[a] Advanced Materials Group (AMG), Department of Mechanical Engineering, Koc University, 34450 Istanbul, Turkey
[b] Center for Integrated Nanotechnology, Los Alamos National Laboratory, Los Alamos, NM, USA
[c] Reactor Materials and Mechanical Design Group, Nuclear Sciences Division, Pacific Northwest National Laboratory, Richland WA 99352, USA
[d] Sigma Division, Los Alamos National Laboratory, Los Alamos, NM, USA

ARTICLE INFO

Keywords:
Machine learning
Multi-principal element alloys
Alloy design
Microstructure
Mechanical properties

ABSTRACT

This study explores the use of machine learning (ML) as a computational tool to accelerate the design of multi-principal element alloys (MPEAs) with improved tensile elongation. An ML model was trained using available experimental data from the literature along with theoretically derived features to predict yield strength (YS) and ductility. A subset of ML-predicted compositions—CoNiVFe, CoNiVTi, CoNiVTiFe, and CoCrNiVTi—was synthesized and evaluated through tensile testing. The ML model underpredicted YS by approximately 20–30 % and overpredicted ductility by 60–70 % for Ti-containing alloys. Microstructural analysis revealed that Ti segregation at interdendritic regions contributed to early fracture, leading to discrepancies in ductility predictions. Ti segregation at these regions likely drives the increased YS due to segregation strengthening. In contrast, the CoNiVFe alloy showed good agreement with both experimental YS and elongation, with prediction errors of ~10.2 % and ~20.7 %, respectively. Microstructural characterization revealed minimal segregation in this alloy, suggesting that the ML model can reliably predict the properties of alloys with little to no segregation. These findings highlight the capability of ML in predicting YS with good accuracy but underscore its limitations in capturing defect-driven failure mechanisms such as segregation-induced embrittlement.

1. Introduction

Traditional engineering alloys, such as stainless steel or Ni-based super alloys, consist of a single-principal element with additional solute elements present in lower amounts than the principal element. On the contrary, multi-principal element alloys (MPEAs) contain three or more principal elements where none of them solely dominates the composition. To elaborate, MPEAs with three to four elements and five or more than five elements are called medium-entropy and high-entropy alloys (MEAs & HEAs), respectively. The entropy concept suggests that the high configurational entropy due to mixing elements with near equilibrium concentrations in MEAs and HEAs results in formation of single-phase solid solutions [1–7]. However, it was also revealed that many HEAs can have a multiphase microstructure; therefore, proving that the high configurational entropy is not the primary factor governing the phase formation dynamics in HEAs [8–10]. Nevertheless, some of the equimolar HEAs were shown to be single-phase face-centered cubic (FCC) or body-centered cubic (BCC) solid solutions [11–13]. Owing to their excellent mechanical properties, corrosion and wear resistance, and microstructural stabilities at elevated temperatures, potential applications of MPEAs in future are still being investigated [14]. More specifically, BCC MPEAs suffers from a lack of room temperature ductility, while FCC ones have low strength. For instance, single FCC phase equimolar CoCrFeNiMn alloy [15] has good tensile ductility at room and cryogenic temperatures but not a high yield strength (YS) [16]. On the other hand, BCC MPEAs have high yield strength (YS) but very limited ductility at room temperatures [17,18]. Thus, investigating and developing new MPEAs with good strength-ductility synergy is an important endeavor.

To accomplish an acceptable strength-ductility synergy in MPEAs, which surpass traditional engineering alloys, researchers have attempted to develop multiple strategies in the literature. For instance, adding

☆ This article is part of a special issue entitled: 'AI Materials' published in Materials & Design.

* Corresponding author.
E-mail address: saryuj@lanl.gov (S.J. Fensin).

https://doi.org/10.1016/j.matdes.2025.114434
Received 18 April 2025; Received in revised form 17 July 2025; Accepted 18 July 2025
Available online 19 July 2025
0264-1275/Published by Elsevier Ltd. This is an open access article under the CC BY-NC-ND license (http://creativecommons.org/licenses/by-nc-nd/4.0/).

or replacing elements and their concentration in different alloy families have been investigated by researchers [19]. Chen et al. reported that addition of Mo into the TiNbZr base-alloy increased compressive YS and hardness drastically but reduced the compressive strain before failure. The strengthening effect was attributed to grain refinement and solid solution strengthening due to Mo addition [20]. In another study, Si addition into to $(VNbTaTi)_{100-x}Si_x$ alloys was investigated and shown that silicide formation in the microstructure resulted in compressive YS to increase from 704 MPa in VNbTaTi to 1671 MPa in $(VNbTaTi)_{90}Si_{10}$, while ductility decreased from >50 % to 12 % [10]. Sheikh et al. also suggested that valence electron concentration (*VEC*) $\leq$ 4.5 can be used to develop intrinsically ductile refractory HEAs [21]. It should be noted that most of these studies using the aforementioned strategies to develop new alloys report compressive mechanical properties, which might not reflect the actual performance of the alloys under tensile loading. An example of this tension–compression asymmetry was shown for $Ti_{1.5}NbVAl_x$ (x = 0.25, 0.5, 0.75, 1) refractory MPEAs, by Zhu et al [22]. To elaborate, while $Ti_{1.5}NbVAl_{0.75}$ and $Ti_{1.5}NbVAl$ showed >50 % strain under compression, they demonstrated 1 and 0 % elongation under tensile load, respectively, suggesting a very brittle fracture behavior [22]. To sum up, developing new MPEAs is complex and burdensome, and multiple factors can affect properties.

Compared to traditional alloys, multiple constituent elements govern the properties of MPEAs, thus, making it harder for researchers to identify the influence of each element separately [23]. Additionally, the vastness of the compositional space, i.e. numerous possible combinations of constituent elements, for any given family of MPEAs makes the development of such alloys by using conventional trial-and-error methods unproductive and expensive [24]. As a solution to this problem, Machine Learning (ML) appears to be an efficient computational tool to unearth the complex and hidden patterns, and implicit connections within a dataset making the design process efficient as opposed to conventional trial-and-error methods [25,26]. Utilization of ML algorithms in materials science has emerged in a variety of optimization problems, including corrosion [27,28], fatigue life [29], Young's modulus [30,31], phase prediction [25,32–34], hardness [35], and YS [36–38]. While there are many works about prediction of mechanical properties for MPEAs, most of them only focused on compressive properties. Furthermore, predicted mechanical properties include YS, ultimate strength, hardness, and Young's modulus, and very rarely elongation.

However, there has been a slight increase in the number of predictions of tensile properties of MPEAs by ML in the literature, especially elongation. One of the first published works belongs to Xu et al., where they utilized gradient-boosting regressor (GBR) to find the optimum composition in the Fe-Cr-Ni family of MPEAs with the best strength-ductility trade-off and ultimate tensile strength. Nevertheless, the actual experimental results were ~30 % lower than the predicted results for all the target properties [39]. In another work, tensile strength and ductility of nitrogen-doped CoCrFeMnNi based HEAs with a dataset consisting of 88 entries were predicted. Although their predictions for tensile YS and ultimate strength agreed with the experimental results, the accuracy of the predicted values in the higher range (i.e., >1000 MPa) was drastically reduced [40]. Additionally, Zhao et al. designed and fabricated three new TiZrNbVAl refractory HEAs with improved elongations up to ~23 % under tensile loading [41]. Other recent examples developing new MPEAs with improved tensile ductility utilizing machine learning can be found in the references [39,42,43]. Therefore, more studies should be published including compressive and tensile properties of new MPEAs to report the degree of tension–compression asymmetry and solve the scarce data problem in reported tensile properties of these alloys.

The goal of this study is to develop a ML model trained on literature data and theoretical features to predict YS and ductility in MPEAs. The compositions predicted by the ML model were experimentally synthesized and evaluated through tensile testing. A comparison between the predicted and experimental results was conducted to assess the accuracy of the model. The ML model accurately predicts YS based on the input features considered in this study. Furthermore, it can reliably predict both strength and ductility when unaccounted factors, such as microstructural segregation, do not significantly influence mechanical properties. While ML has demonstrated potential in accelerating alloy design, its accuracy remains limited by the absence of critical microstructural parameters such as grain size, solute segregation, dislocation density, and precipitation effects. Incorporating these factors into predictive frameworks is essential for improving the reliability of ML models in alloy design.

2. Methods

2.1. Computational details

To develop new MPEAs with optimum strength-ductility synergy, a dataset for training a ML model was constructed. The dataset that we used herein is taken from [5], published by Borg et al. in 2020 featuring compilation of mechanical properties of 630 MPEAs. The original dataset contains 1545 records, of which 792, 358, and 395 present compression, tension, and hardness data, respectively. As our aim was to predict tensile properties of MPEAs, only tensile part of this dataset was used. However, the original dataset from Borg et al. [5] contains 30 different elements, various processing methods (i.e., annealing, cold-rolling, hot isostatic pressing etc.) and production methods (Vacuum arc-melting (VAM), ball milling etc.). Since for small datasets, having a high number of input variables in the training dataset would affect the accuracy of the predictions, we applied some restrictions to the training dataset to align with the aim of this work. The restrictions that we implemented were as follows: (1) eliminated rare-earth elements, or elements that we did not want to include in our final dataset; (2) only considered tensile data as mentioned before; (3) considered only alloys manufactured using VAM; and (4) only annealing or cold-rolling as additional processing methods in addition to alloys in as-cast condition. Furthermore, it should be noted that alloys with the same chemical composition with different experimentally measured YS and ductility values between different papers were added to our dataset as one entry after the YS and ductility were averaged. The final dataset consisted of 117 datapoints (30 of 117 datapoints were included by the authors from papers published after 2020, manually [22,44–55]) and included twelve elements: Al, Co, Cr, Cu, Fe, Mn, Mo, Nb, Ni, Ti, V, and Zr; along with four experimental parameter: processing method, annealing temperature, annealing time, and testing temperature at which the mechanical tests were performed.

It has been reported previously that modeling the underlying relationship between the target properties (YS and ductility in this work) and alloy chemical compositions might not be enough to establish an accurate relationship between the input and target properties [28,30,56]. This implies that information in addition to the chemical composition that will aid the ML models to establish the relationships between the input data and target properties are needed. Hence, calculating new empirical features from the constituent elements' physical and chemical properties is necessary. In the present study, there are 34 calculated empirical features in addition to twelve elements and four experimental parameters. The calculated empirical features include the most encountered features in literature, such as Valence Electron Concentration (*VEC*), the atomic size difference (δr), the difference in electronegativity ($\Delta\chi$), the mixing enthalpy (ΔH), the configurational entropy (ΔS) [57], the $\wedge$ parameter designed by Singh et al. [58], the γ parameter suggested by Wang et al. [59]. We also employed parameters from strengthening theory, such as, the local size mismatch (*D.r*), the energy term in the strengthening model (*A*), and the Peierls-Nabarro factor (*F*) [60,61]. The complete set of features, as demonstrated in Fig. 1, along with their definitions and formula are presented in Supplementary Information Table S1. It should be noted that we prepared

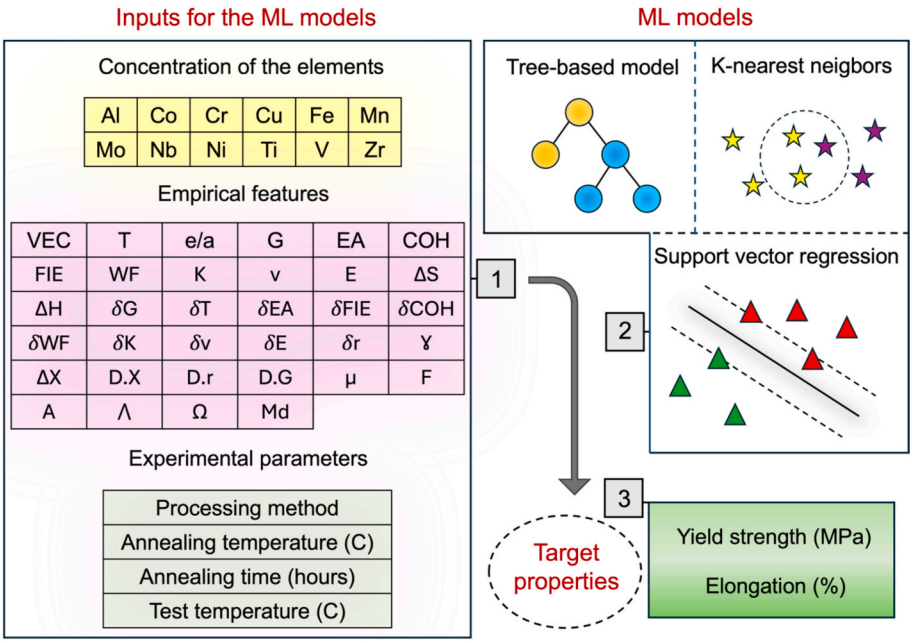


Fig. 1. Schematic diagram for the present work. The complete set of input features (i.e., concentration of the elements, empirical features, and experimental parameters), along with the main ML algorithms utilized in this work and target properties that were predicted.

two different datasets: one with tensile ductility and the other with YS as the target properties. Therefore, we will share the results corresponding to predictions of both tensile ductility and YS datasets.

As mentioned above, we have a total of 50 input variables (12 elements with their concentration for each alloy in the dataset, 34 calculated empirical features, and four experimental parameters), which increases the degrees of freedom of the ML models. To be more specific, a high number of input variables becomes a troublesome issue in the case of using scarce datasets. One of the problems that should be addressed when handling high number of input variables is to identify highly correlated features because high correlation among features causes multicollinearity, degrading model performance and the accuracy of the predictions [28,30,62]. In other words, highly correlated features are duplicate information in the datasets. Hence, a correlation screening was performed to identify the highly correlated features (features include chemical composition and empirical features and exclude experimental parameters in the correlation screening step) in our dataset [63]. We used the Pearson correlation coefficient (PCC) with a 0.95 threshold to identify the highly correlated features. Once correlated features were identified, we retained the one with higher importance [64]. To estimate the importance of each feature, Shapley additive explanations (SHAP) analysis developed by Lundberg and Lee was employed [65]. The model we utilized while estimating the importance of the features was the Random Forest (RF) algorithm. This was the first feature elimination step that was performed before evaluating the ML model performance.

Following, we employed k-nearest neighbors (KNN), RF, GBR, support vector regression with a polynomial kernel (SVR-P), and support vector regression with a radial basis kernel (SVR-R) to construct predictive models using our input variables. Deep learning methods were not used in the current study as they require a much higher amount of training data [66]. Bayesian optimization was implemented to tune the hyperparameter of the aforementioned algorithms [26]. To normalize data and eliminate any existing skewness problems in the dataset, a standard normalization method was applied to the dataset, normalizing the data around zero mean and one standard deviation. To evaluate models' performance, we used 5-fold cross-validation (CV), and the mean absolute error (MAE) was selected as the error metric for the comparison and evaluation of the models.

Once we selected the best-performing models out of the five models employed, we performed a second feature elimination, which is forward feature selection (FFS). Feature elimination process is one of the most important steps while building a predictive model, especially in the case where scare data is being used. Since the higher the number of features in a dataset, the more overfitting will take place during the training of ML models, resulting in deterioration in the generalization capability of the models. Hence, to avoid overfitting and obtain a robust ML model, the best feature set should be selected eliminating all the redundant features. In the present study, FFS was utilized to obtain the best subset of features describing target variables ductility and YS (note that we performed all steps explained above from the beginning while building the final models for both ductility and YS). FFS is a method that iteratively builds a model by adding one feature at each iteration, choosing the one maximizing the MAE score in each iteration [67]. Then, the best subset of features leading to a minimum MEA score is selected. After the best subset was selected, Bayesian optimization was implemented once again to tune the hyperparameters of the final models to enhance the performance of the ML algorithm.

Lastly, hypothetical search spaces were created for four different alloy families, namely, CoNiVFe, CoNiVTi, CoNiVTiFe, and CoCrNiVTi, to predict the ductility and YS and search for the optimum compositions within each family. Based on the minimum and maximum values for each element in the dataset, the following lower and upper boundaries were defined: $5 \leq Co \leq 45$, $5 \leq Cr \leq 45$, $0 \leq Fe \leq 45$, $5 \leq Ni \leq 50$, $0 \leq Ti \leq 45$, $5 \leq V \leq 35$, while building the hypothetical search spaces. Furthermore, the elemental concentration was increased with a one at% step size within the lower and upper boundaries. As a results, we obtained 42191, 42191, 1456411, 1243286 different alloy compositions CoNiVFe, CoNiVTi, CoNiVTiFe, and CoCrNiVTi, respectively. Since the number and concentration of the constitutive elements for some of the alloys in these hypothetical search spaces do not comply with the official composition-based HEA definition (between 5 and 35 at%), we will define them as MPEAs. After the hypothetical search space was created for the alloy families, the empirical features were also estimated as they were also necessary to be used as input for the predictions. The experimental parameters for the compositions in the hypothetical search space; processing method, annealing temperature, annealing time, and testing temperature were set to as-cast, zero for annealing temperature

and time (i.e., no annealing), and 25 °C. Subsequently, the compositions in the hypothetical search spaces were fed into the best ML model to make ductility and YS predictions for the unknown compositions in the hypothetical search spaces, CoNiVFe, CoNiVTi, CoNiVTiFe, and CoCrNiVTi, respectively. To estimate the uncertainty of the predictions, we utilized bootstrapping method by resampling the data from the original training data with replacement. In other words, we trained our models on 100 bootstrapped training datasets to acquire 100 predictions for each composition in our hypothetical search spaces. After predicting ductility and YS for CoNiVFe, CoNiVTi, CoNiVTiFe, and CoCrNiVTi family of alloys, we sorted them based on the ductility and selected the composition with the highest elongation, as this was the most significant property we aimed to optimize. We also reported YS predictions along with ductility predictions.

2.2. Experimental details

Bulk materials of the selected conditions were synthesized via arc melting using a Materials Research Furnace arc-melting system which uses a water-cooled copper hearth. The chamber was pumped down to 5 $\times$ 10^{-6} torr through three cycles of evacuation and purging with high-purity argon gas to create an inert atmosphere. Final chamber pressure was 200 torr. Before melting the samples, a titanium getter was melted for 60 s. Pure elements with 99.99 % purity or better were used for synthesis, with each element measured to an accuracy of ±0.1 wt% to ensure the targeted composition was met. Each synthesized material underwent six remelting cycles at 300 Amps, flipping the button each time, to promote homogeneous mixing. Moreover, the total mass of the pure elements measured before melting was within 0.5 wt% of the final mass, indicating that no significant elemental losses occurred during the melting process.

The microstructure of the manufactured materials was characterized using standard metallographic techniques. The blank was sectioned to investigate the microstructure in the in-plane (IP) and through-thickness (TT) directions. The samples were cold mounted in epoxy and prepared simultaneously with the Struers LabPol-30 automatic grinder/polisher. The samples were mechanically ground using silicon carbide paper using a grit of 280 to 5000. This was followed by final polishing using a 0.5-μm alumina and 0.05-μm colloidal silica solution. Prior to microscopy, specimens were cleaned and rinsed with isopropanol.

An Apreo 2 SEM, equipped with an Oxford Electron Back Scatter Diffraction (EBSD) detector, was used to collect EBSD patterns/images with an accelerating voltage of 20 kV and beam current of 13 nA. Post processing of EBSD images was conducted using AZtec Crystal and consisted of cleaning images using zero solution removal with four iterations and a nearest neighbor requirement of 5 pixels.

Tensile samples were machined using electrical discharge machining (EDM) producing the geometry shown in Fig. 2. Specifically, the gage length was measured from the transitions from straight to curved along the length of the sample using a Mitutoyo TM-100 tool makers microscope. Sample width and thickness were measured at 3 locations along the gage length and in the center using Mitutoyo TM-100 tool makers microscope. Post-test analysis of the test data was performed using the dimensions closest to failure location.

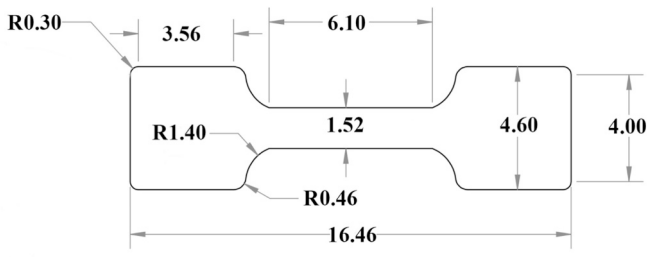


Fig. 2. Tensile specimen geometry. Dimensions are shown in millimeters. Thickness is 1.27 mm.

Tests were conducted at room temperature on an MTS 880 servo-hydraulic load frame that was programmed to run each test at the desired "true strain rate" of 10^{-3} s^{-1} in tension. The true strain rate test is achieved by changing the displacement rate every 0.5 % strain to accommodate changing dimensions during the tests. Data was collected from the computer clock, time (sec.), the LVDT (mm), an extensometer (mm) and the system load cell (N) having a 100 kN capability and a10kN load cell for the collected data. The extensometer was attached to the test grips using rubber bands. A small layer of paint was applied to the grips where the extensometer knife edge made contact to increase the contact friction and reduce the chance of slipping. The standard equations were used to calculate the stress/strain response of each sample using the measured values for gage length and gage width. In this work we report YS and strain to failure for all samples.

3. Results

3.1. Computational results

First, the features with high correlation were removed using PCC method. Since we have 50 input variables, we selected the ones that are highly correlated and present them in Fig. 3a1 and b1 for tensile ductility and YS datasets, respectively. A 5-fold CV was utilized during estimation of the importance of each feature, where RF model was employed, and importance of the features were calculated using SHAP analysis. The same color code represents the two highly correlated features. Out of two highly correlated features, we eliminated the one with lower importance. After, first feature elimination step is completed, KNN, GBR, RF, SVR-P, and SVR-R models were tested to evaluate their predictive performances. The performance of the models was evaluated based on MAE metric and compared as shown Fig. 3a2 and b2 for tensile ductility and YS prediction. It should be noted that the performance trends were the same for both tensile ductility and YS predictions. KNN and GBR models resulted in high overfitting during the training (i.e., the higher the difference between the training and testing set is, the worse the model's predictive performance will be due to overfitting). Especially, the KNN model had zero training set error, suggesting that the model fit the training data perfectly, i.e. its generalization capability for the unseen data will be very poor. The training and testing errors for SVR-P model were higher compared to all other models, pointing out that a case of underfitting, where the SVR-P models fail to fit the data. Finally, SVR-R and RF models performed better than other models for tensile ductility (Fig. 3a2) and YS (Fig. 3b2) predictions, respectively. Since both SVR-R and RF had similar errors for ductility and YS predictions, we kept both models for further evaluation, because one of them might perform better after we performed further feature elimination using FFS.

Following the evaluation of the model performances, we implemented the FFS process to eliminate more redundant features from the datasets for both SVR-R and RF models. However, it is important to mention that before FFS process was performed, we evaluated whether utilizing chemical composition of the elements enhanced model performances or not while predicting elongation. Based on Supplementary Information Fig. S1, there was no improvement or deterioration in the performance of the SVR-R and RF models for ductility predictions. Hence, to avoid overfitting more and decreasing the complexity of the models further, we eliminated chemical composition of the elements and only used empirical features and experimental parameters to predict ductility. Such an approach, i.e. only using calculated empirical features as input to train an ML model, was also used before in the literature [56,68]. It should be noted that the experimental parameters: processing method, annealing temperature, annealing time, and test temperature were fixed as a group to be included in the final feature space at the onset of the FFS process. The FFS process of SVR-R and RF models for tensile ductility predictions is shown in Fig. 4a1 and a2, respectively.

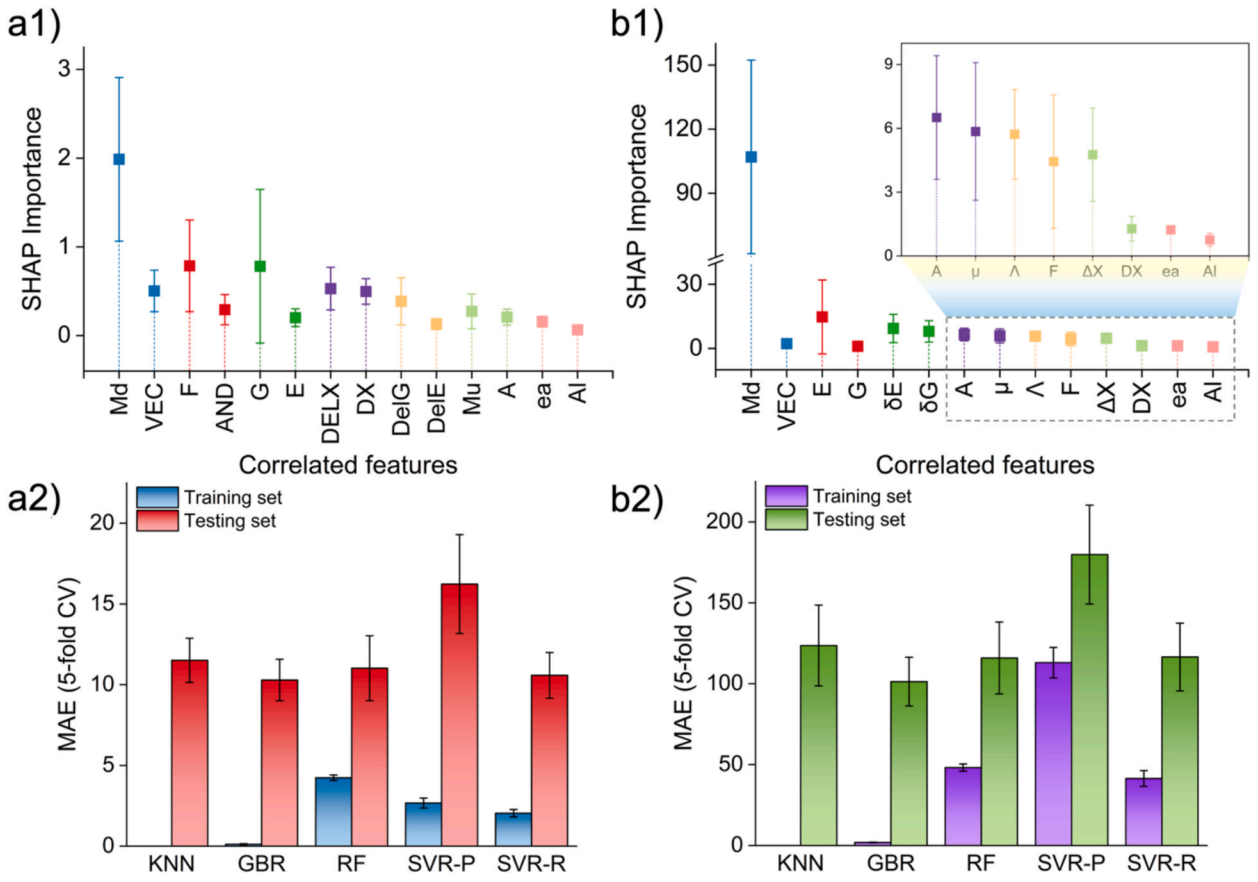


Fig. 3. (a1) The SHAP importance of the highly correlated features and (a2) comparison of the ML models used for prediction of tensile ductility with 5-fold CV. (b1) The SHAP importance of the highly correlated features and (b2) comparison of the ML models used for prediction of tensile YS with 5-fold CV.

The error was the highest, when only four experimental features were utilized during the training. As more features were included as inputs into the models, the error first decreased and then leveled off for both SVR-R and RF models in Fig. 4a1 and a2. The red stars in Fig. 4a1 and a2 represent the best feature subset, which gave the least error. After the best subset of features selected by FFS, Bayesian optimization was implemented to tune the hyperparameters of the models. Once the models were trained with the selected subset and optimized hyperparameters for each model, SVR-R model was chosen to be the final algorithm as it performed better than SVR-R for tensile elongation predictions, as demonstrated in Fig. 4a3. The best feature subset and optimized hyperparameters can be found in Supplementary Information Table S2 for modeling of elongation data.

Whether utilizing the chemical composition of the elements enhanced model performances or not was also evaluated for YS predictions. Based on Supplementary Information Fig. S1, an improvement was observed in the performance of the SVR-R and RF models for YS predictions when composition was included in the input data. Thus, the chemical composition of the elements, empirical features and experimental parameters was utilized to predict YS as opposed to the case in elongation predictions where the chemical composition of the elements was not included as input to the ML algorithms. Similar to the FFS process for tensile ductility predictions, the experimental parameters: processing method, annealing temperature, annealing time, and test temperature were fixed as a group to be included in the final feature space at the onset of the FFS process for YS predictions, too. The FFS process of SVR-R and RF models to predict tensile YS is shown in Fig. 4b1 and b2, respectively. After the best subset of features selected by FFS, Bayesian optimization was implemented to tune the hyperparameters of the models.

Once the models were trained with the selected subset and optimized hyperparameters for each model, RF model was chosen to be the final algorithm as it performed better than SVR-R to predict YS, as demonstrated in Fig. 4b3. The best feature subset and optimized hyperparameters can be found in Supplementary Information Table S3 for YS predictions.

To demonstrate the prediction performance of models, the parity plots are presented in Fig. 4a4 and b4, comparing experimental values to predicted ones, for elongation and YS predictions, respectively. The R^2 values, showing goodness of fit, were higher than 0.8 for both elongation and YS predictions indicating a good/acceptable prediction performance. While the models predicted multiple compositions to meet a good ductility and YS combination, only a handful were selected for actual manufacturing. Though it should be noted that the main focus was to find the optimum alloys with the best tensile elongation, we also predicted YS values to make an informed decision regarding the ductility-strength synergy. The selected compositions are tabulated in Table 1 along with the predicted YS and elongation (%) results. Specifically, these compositions were selected because of their high ductility accompanied by good YS predictions.

3.2. Experimental results

3.2.1. Grain structure and phase analysis

The predicted compositions were fabricated using arc melting and subsequently machined into tensile samples. The grain structure of the MPEAs was characterized using Electron Back Scatter Diffraction (EBSD). The inverse pole figure (IPF) and pole figure (PF) maps of the alloys are shown in Fig. 5. The inset in Fig. 5a displays a machined dog bone specimen obtained from the arc-melted samples. The blue-colored plane marked in the arc-melted samples was used for characterization. This plane was selected because it is perpendicular to the solidification

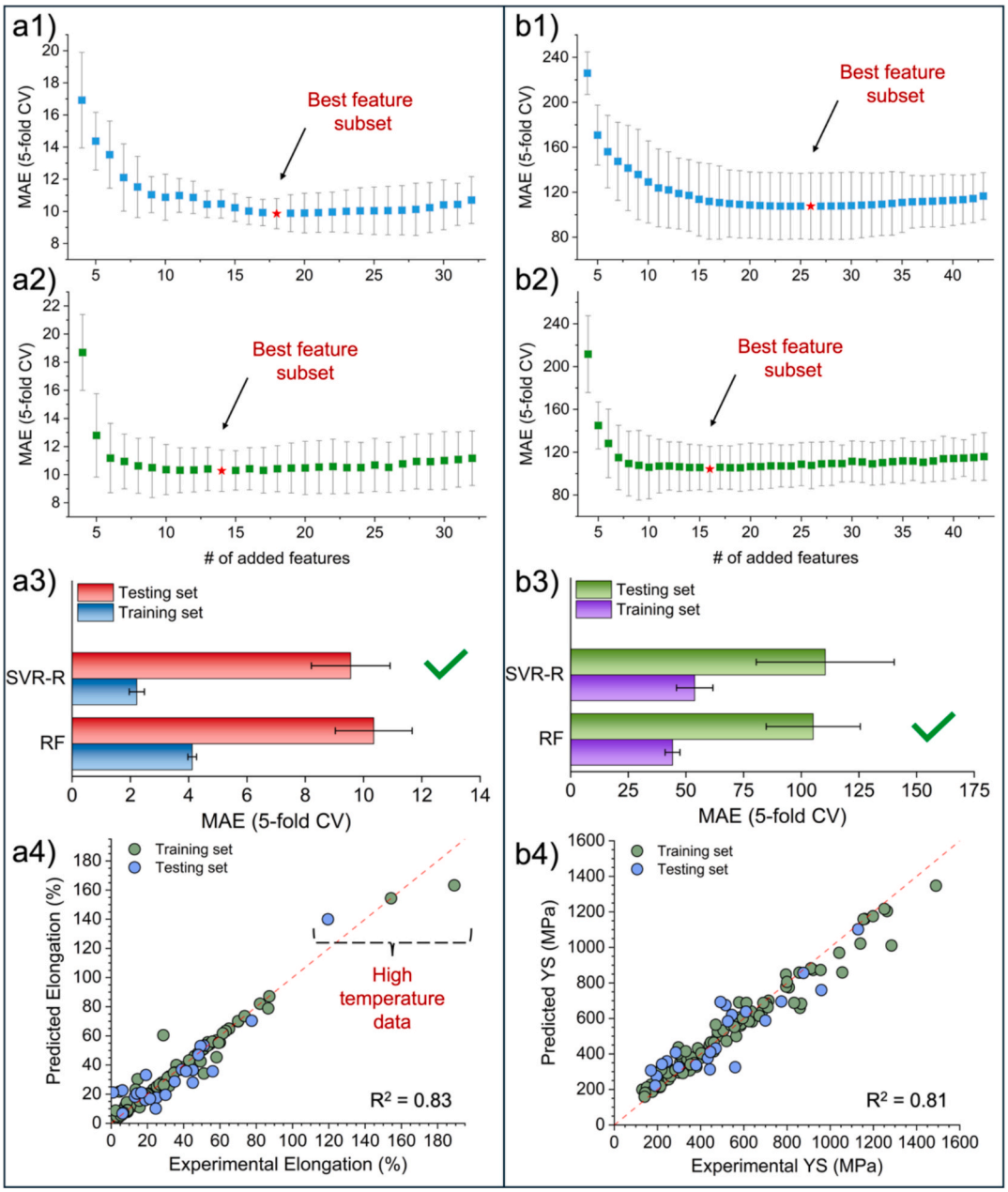


Fig. 4. FFS process for (a1) SVR-R and (a2) RF models, with red stars indicating the best feature subset. (a3) Model performance for elongation prediction, showing SVR-R outperforms RF. (a4) Parity plot for elongation predictions using SVR-R (80:20 training/testing split); three high-temperature data points are noted on the right. FFS process for (b1) SVR-R and (b2) RF models for YS prediction. (b3) Model performance, showing RF outperforms SVR-R. (b4) Parity plot for YS predictions using RF. (For interpretation of the references to color in this figure legend, the reader is referred to the web version of this article.)

Table 1
The selected compositions and predicted elongation (%) and YS (MPa) values.

MPEAs	Elements (at%)					Elongation (%)	YS (MPA)
MPEA-1	Co (28)	Ni (40)	V (23)	Fe (9)		62.3 ± 12.4	401 ± 84
MPEA-2	Co (43)	Ni (34)	V (18)	Ti (5)		62.3 ± 13.6	529 ± 95
MPEA-3	Co (15)	Ni (46)	V (12)	Ti (5)	Fe (21)	71.5 ± 13.3	515 ± 87
MPEA-4	Co (42)	Ni (32)	V (12)	Ti (7)	Cr (7)	65.8 ± 11.4	526 ± 79

direction, and tensile loading is performed parallel to this direction. As a result, it provides a cross-sectional view of the solidified grains.

All four alloys exhibited a strong (100) crystallographic texture along the solidification direction, with a texture intensity ranging from approximately 7 to 9 multiples of random distribution (MRD). This preferred texture is a direct consequence of the solidification behavior of FCC metals. In FCC materials, the (100) planes have the lowest surface energy, making them thermodynamically favorable for solidification [69]. During directional solidification, grains with a (100) orientation aligned with the heat extraction direction grow preferentially, whereas other orientations are less competitive due to their higher interfacial energy and slower growth rates. Consequently, the solidification process naturally promotes a strong (100) texture along the thermal gradient.

The grain size statistics of the four alloys are shown in Table 2. The mean grain diameter across the alloys ranges from 38 μm (MPEA-2) to

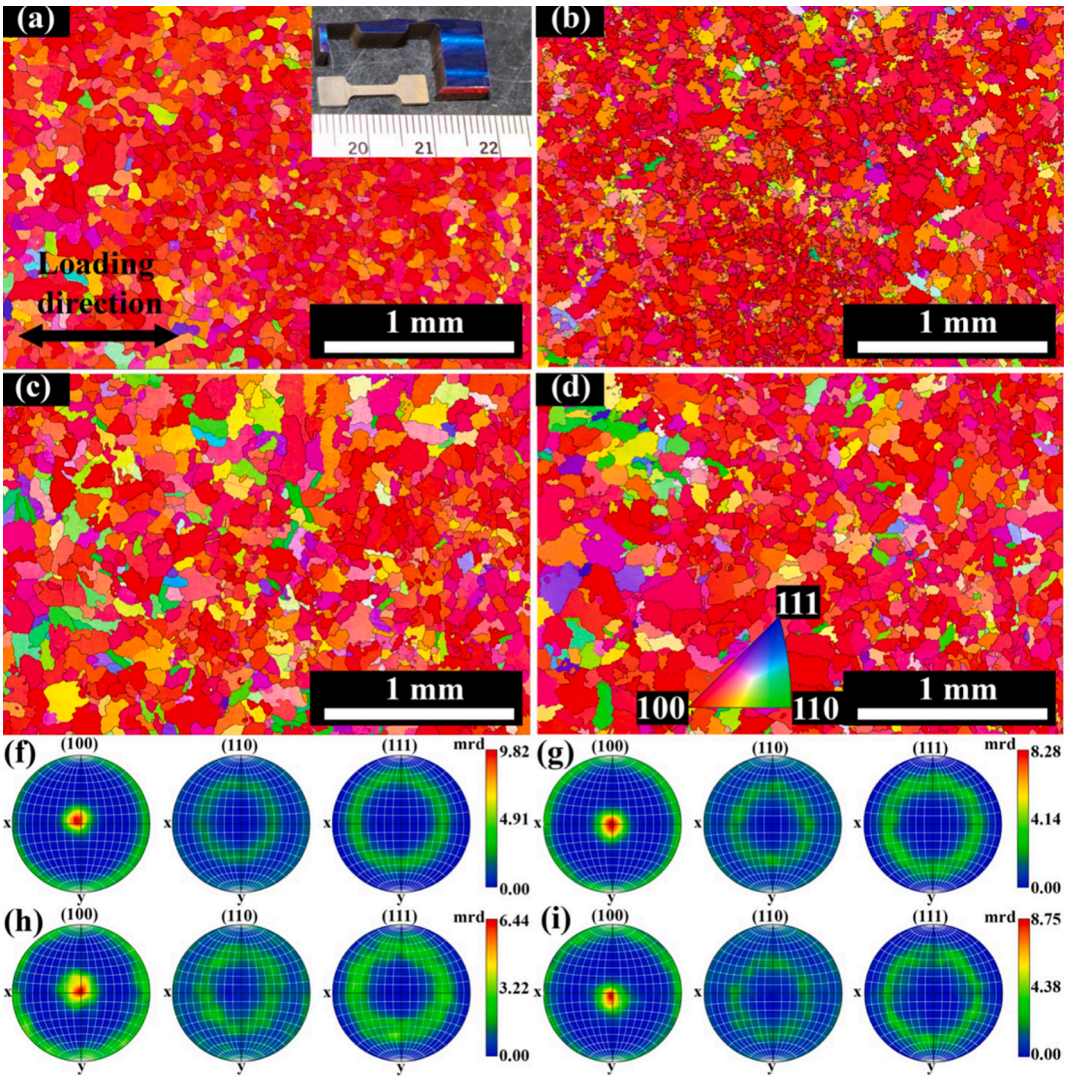


Fig. 5. (a, f) MPEA-1, (b, g) MPEA-2, (c, h) MPEA-3, and (d, i) MPEA-4. The inset in (a) shows a machined dog bone specimen. The blue plane was used for data collection. (For interpretation of the references to color in this figure legend, the reader is referred to the web version of this article.)

Table 2
Grain size statistics of the fabricated MPEAs.

Alloy	Mean grain diameter (μm)	Area weighted mean (μm)	STD (μm)	Maximum diameter (μm)
MPEA-1	61	97	33	230
MPEA-2	38	86	31	205
MPEA-3	64	121	44	280
MPEA-4	59	123	43	370

64 μm (MPEA-3), with MPEA-3 exhibiting the largest average grain size. The area-weighted mean grain diameter, which accounts for the disproportionate influence of larger grains, is significantly higher than the arithmetic mean for all alloys. This suggests a heterogeneous grain size distribution with a mix of fine and coarse grains. Notably, MPEA-3 and MPEA-4 have the highest area-weighted mean diameters of 121 μm and 123 μm, respectively, indicating the presence of large grains that contribute significantly to the overall distribution. This is evident in the IPF maps shown in Fig. 5 as well.

The standard deviation (STD) values further highlight the degree of grain size variation within each alloy. MPEA-3 and MPEA-4 exhibit the highest standard deviations (44 μm and 43 μm, respectively), implying a broader distribution of grain sizes compared to MPEA-1 and MPEA-2. Additionally, the maximum grain diameters reinforce this trend, with MPEA-4 displaying the largest grain recorded at 370 μm, followed by MPEA-3 at 280 μm. In contrast, MPEA-1 and MPEA-2 have smaller maximum grain sizes of 230 μm and 205 μm, respectively.

3.2.2. *Mechanical response*

Fig. 6a and b show the engineering stress–strain and true stress–-strain curves for MPEA-1, MPEA-2, MPEA-3, and MPEA-4. The corresponding experimental yield strength (YS) and elongation values are summarized in Table 3. According to Table 3, MPEA-1 exhibited a YS of 364 MPa and a strain to failure of approximately 78.6 %. While the experimental YS value closely matches the prediction from the ML model, the measured elongation was higher than the predicted value for MPEA-1.

In contrast, replacing Fe with Ti in MPEA-2 resulted in an increase in YS but led to a significant reduction in ductility to just 5 %. While the YS aligns well with the ML model's prediction, the ductility deviates significantly. The addition of Fe into the CoNiVTi system, forming MPEA-3, led to a decrease in YS and a slight increase in elongation compared to MPEA-2. Finally, replacing Fe with Cr in MPEA-4 resulted

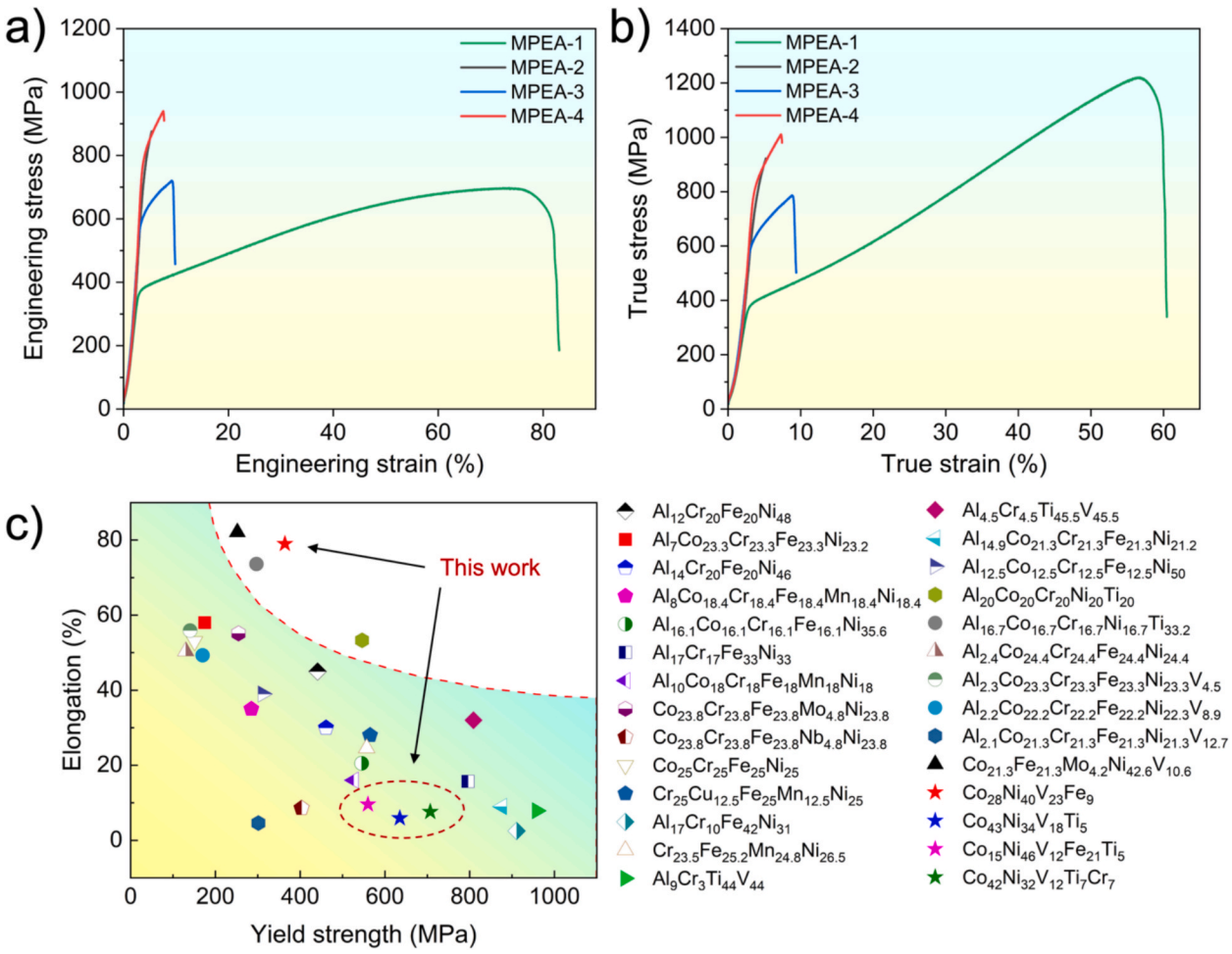


Fig. 6. Mechanical response of MPEA-1, MPEA-2, MPEA-3, and MPEA-4. (a) Engineering stress–strain curves and (b) true stress–strain curves. (c) Comparison of mechanical properties of designed MPEAs with other MPEAs reported in the literature (the data and references for the MPEAs utilized for comparison can be found in Supplementary Information Table S4).

Table 3
Predicted and experimental ductility and YS measurements of the MPEAs at room temperature.

MPEAs	Predicted		Experimental	
	Elongation (%)	YS (MPa)	Elongation (%)	YS (MPa)
MPEA-1	62.3 ± 12.4	401 ± 84	78.6 ± 8.5	364 ± 9.2
MPEA-2	62.3 ± 13.6	529 ± 95	5.9 ± 0.9	635 ± 32.3
MPEA-3	71.5 ± 13.3	515 ± 87	9.6 ± 1.6	560 ± 15.0
MPEA-4	65.8 ± 11.4	526 ± 79	7.6 ± 3.4	707 ± 11.2

in an increase in YS and a reduction in elongation compared to MPEA-3. Overall, the addition of Ti to the alloy system significantly reduced ductility while providing moderate gains in YS.

Moreover, the higher-than-predicted YS in MPEA-2 to MPA-4 suggests that these alloys do not fail prematurely due to defects. If failure were defect-driven, both YS and elongation would be lower than expected. However, since MPEA-2 to MPEA-4 exhibit higher YS than theoretical predictions, additional strengthening mechanisms must be present in these alloys. These mechanisms, however, likely compromise ductility due to the strength-ductility trade-off.

Fig. 6c compares the combination of strength and ductility in these alloys with other MPEAs reported in the literature, containing similar elements to those of the ones utilized herein (the data and references of the MPEAs taken from literature can be found in Supplementary Information Table S4). MPEA-2 to MPEA-4 exhibit a pronounced strength-ductility trade-off, where the increase in strength comes at the expense of ductility. However, MPEA-1 demonstrates an improved balance of strength and ductility, surpassing many of the HEAs previously reported. For instance, MPEA-1 possess a better YS compared to $Co_{21.3}Fe_{21.3}Mo_{4.2}Ni_{42.6}V_{10.6}$ [70] and $Al_{16.7}Co_{16.7}Cr_{16.7}Ni_{16.7}Ti_{33.2}$ [54], while they all share similar elongation capability. This suggests that the proposed ML approach has the potential to identify alloys with exceptional performance. However, the discrepancies observed in MPEA-2 to MPEA-4 are likely due to additional strengthening mechanisms, such as precipitation strengthening and dislocation interactions, which are not accounted for in the ML model.

3.2.3. *Effect of secondary phases and elemental segregation on fracture behavior*

To gain insights into the origin of brittle failure observed in MPEA-2 through MPEA-4, we analyzed the phase constitution and elemental distribution using EBSD and EDS data shown in Fig. 7. These maps reveal the segregation behavior of alloying elements alongside the crystallographic and phase information. A clear distinction can be made between MPEA-1 and the other three alloys in terms of secondary phase formation and elemental segregation.

In MPEA-1, EDS maps show relatively uniform elemental distributions, with only evidence of V segregation. Correspondingly, EBSD phase mapping detected a fully single-phase FCC matrix, with no evidence of secondary phases (Fig. 7e). The IPF map (Fig. 7f) further confirms an equiaxed grain structure without notable intragranular features. This is

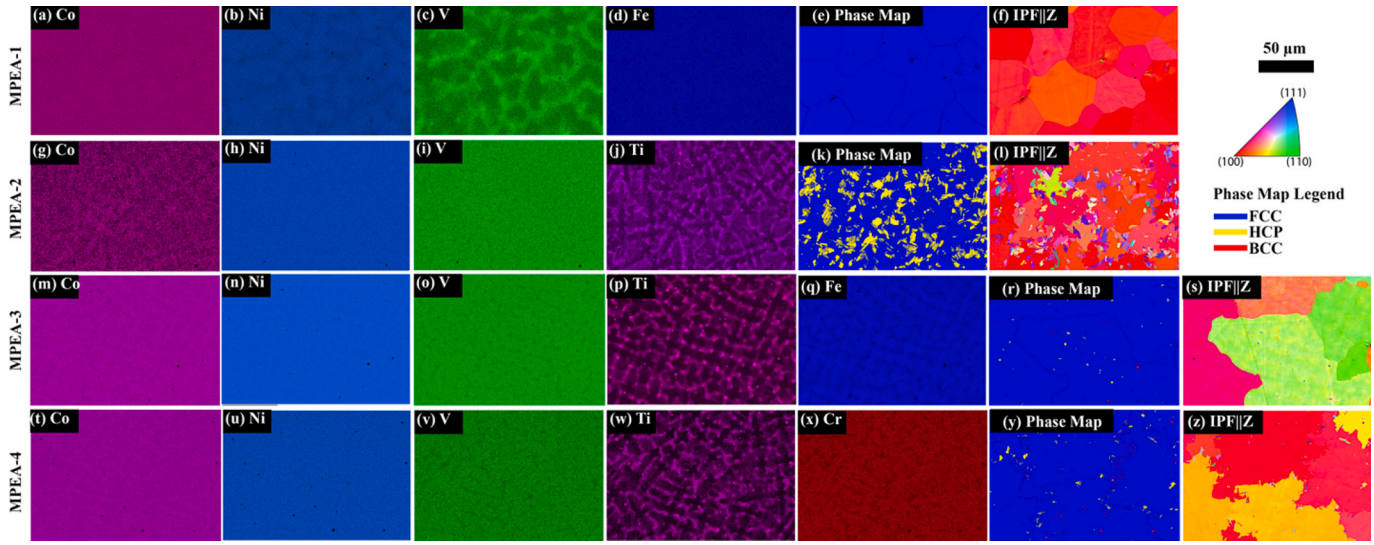


Fig. 7. *EDS and EBSD maps of MPEA-1 to MPEA-4 showing Ti segregation and secondary phase formation.* MPEA-1 shows no secondary phases and minimal segregation. MPEA-2 exhibits ~17 % HCP phase in Ti-rich regions, while MPEA-3 and MPEA-4 show ~1 % HCP or BCC phases aligned with Ti-enriched interdendritic areas.

consistent with the alloy's ductile fracture behavior and the accurate match between its predicted and experimental mechanical properties.

In contrast, MPEA-2 exhibits significant Ti segregation, forming a network-like morphology at interdendritic regions (Fig. 7j), which strongly correlates with the presence of ~17 % secondary HCP phase indexed as Ti-hexagonal. The phase map (Fig. 7k) highlights these regions, indicating transformation from the matrix FCC phase to HCP domains. These secondary phases are largely confined to the Ti-rich interdendritic regions, implying that localized phase decomposition has occurred due to the thermodynamic instability introduced by Ti accumulation. The presence of HCP phases is known to impede dislocation motion due to their limited slip systems, and their spatial confinement to Ti-segregated boundaries further enhances stress localization, making these regions likely crack initiation sites.

MPEA-3 and MPEA-4 also demonstrate Ti-rich interdendritic segregation (Fig. 7p, w), albeit with significantly reduced secondary phase volume fractions compared to MPEA-2. EBSD phase maps (Fig. 7r, y) indicate the presence of HCP or BCC phases at a volumetric fraction of ~1 %. While these fractions are lower, their presence at structurally and chemically weakened boundaries—compounded by elemental depletion of other strengthening elements (Co, V, Cr)—suggests they may still act as preferential crack nucleation points. The brittleness observed in these alloys despite limited secondary phase content may thus arise from a combined effect of segregation-induced embrittlement and local phase incompatibility.

The spatial correlation between Ti enrichment and secondary phase formation across MPEA-2 to MPEA-4 provides a mechanistic pathway for early failure. These secondary phases not only reduce local ductility

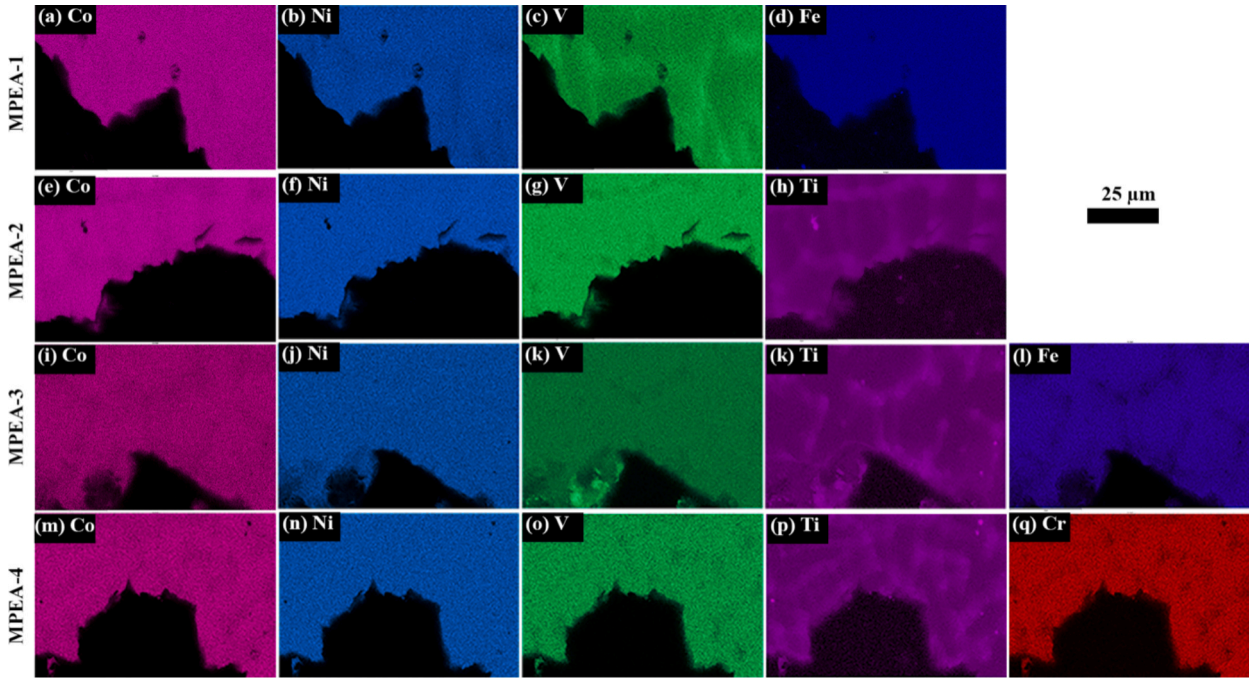


Fig. 8. Element segregation profiles at the fracture surface of the MPEAs. (a–d) MPEA-1, (e–h) MPEA-2, (i–l) MPEA-3, (m–q) MPEA-4 Ti maps of MPEA-2 to MPEA-4 show that fracture is occurring along the Ti segregated boundaries.

but also generate elastic mismatch and interfacial stress concentrations under mechanical loading. This interplay between chemical inhomogeneity and microstructural evolution highlights the critical role of segregation-driven phase separation in deteriorating the mechanical integrity of these MPEAs.

Building on the microstructural evidence of Ti-induced secondary phase formation, we further investigated the origins of reduced ductility in MPEA-2 through MPEA-4 by performing EDS analysis near the fracture surfaces. Fig. 8 presents the elemental segregation profiles across the fracture surfaces of the four MPEAs.

In MPEA-1, consistent with its chemically homogeneous microstructure and absence of secondary phases, the fracture surface revealed minimal elemental segregation. Only weak V segregation was detected, and the fracture path did not correlate spatially with these regions. This suggests that stress concentration at such segregation boundaries is negligible and unlikely to contribute significantly to crack initiation or propagation. As a result, MPEA-1 maintains good ductility and displays excellent agreement between predicted and experimentally measured mechanical properties.

In sharp contrast, MPEA-2 to MPEA-4 exhibit pronounced Ti segregation at interdendritic regions, which align closely with their respective fracture paths. These Ti-enriched zones coincide with the secondary HCP or BCC phases identified in EBSD phase maps, underscoring a strong correlation between phase decomposition and fracture localization.

The alignment of the fracture surfaces with these segregated and phase-transformed regions suggests that they serve as preferential crack initiation sites. Additionally, these segregation profiles are known to hinder dislocation mobility, contributing to a form of segregation-induced strengthening. While this may account for the elevated strength observed in MPEA-2 to MPEA-4, it comes at the cost of reduced ductility and early failure under mechanical loading [71–74]. Supplementary Information Figs. S2 and S3 further illustrate the brittle fracture morphology and pronounced crack marks in these alloys, reinforcing the role of Ti-rich secondary phase regions in fracture behavior.

4. Discussion

4.1. Limitations of machine learning predictions and the role of microstructural effects

The discrepancies between the predicted and experimental values of yield strength (YS) and ductility for MPEA-2, MPEA-3, and MPEA-4 can be attributed to several factors, primarily the lack of microstructural information in the dataset. The current ML model is trained on literature data that mainly includes composition and processing details but lacks information on key microstructural features such as grain size, dislocation density, solid solution effects, and precipitation behavior. This limitation arises because literature studies often do not provide in-depth microstructural characterization, leading to an assumption that all vacuum arc melted (VAM) alloys are homogeneous. However, variations in processing parameters and solidification conditions can lead to significant differences in strengthening mechanisms, which directly affect mechanical properties but are not captured by the model.

The yield strength of an alloy is determined by multiple strengthening mechanisms, expressed as [71,74–76]:

$$\sigma_y = \sigma_o + \sigma_{SS} + \sigma_{GB} + \sigma_{PPT} + \sigma_{TW} + \sigma_{Dis} \quad (1)$$

where σ_o represents the intrinsic strength of the lattice, while the other terms correspond to solid solution strengthening (σ_{SS}), grain boundary strengthening (σ_{GB}), precipitation strengthening (σ_{PPT}), twin boundary strengthening (σ_{TW}), and dislocation strengthening (σ_{Dis}). Each of these mechanisms plays a role in determining the final mechanical properties of the alloys.

While grain boundary strengthening [16] is often significant, as described by the Hall-Petch relationship,

$$\sigma_{GB} = \sigma_o + k_y/\sqrt{d} \quad (2)$$

where k_y is the Hall-Petch coefficient and d is the mean grain diameter. Since the mean grain sizes of these alloys are within a comparable range, grain size effects on strength are expected to be similar across all alloys. However, k which governs how effectively grain boundaries hinder dislocation motion, is influenced by solute segregation, grain boundary chemistry, and atomic interactions, further contributing to variations in mechanical properties [77–80].

One of the key contributors to mechanical differences is solid solution strengthening (σ_{SS}), which arises from atomic size mismatch and electronic interactions between alloying elements [71,74,81,82]. The observed Ti segregation and Co, V, Fe, and Cr depletion in interdendritic regions suggest that solid solution strengthening contributions vary across different regions of the microstructure. Ti segregation at interdendritic regions disrupts local atomic arrangements and alters dislocation interactions. The failure in MPEA-2 to MPEA-4 was influenced by Ti segregation patterns. Unlike MPEA-1, where the fracture surface did not strictly follow the weak segregation profile, these three alloys showed a strong correlation between fracture surface and Ti-segregated boundaries. Ti segregation affects mechanical properties in two ways. It creates localized stress concentrations at interdendritic regions including grain boundaries, promoting crack initiation and reducing ductility. It also contributes to segregation strengthening, where solute-enriched regions hinder dislocation motion, increasing yield strength at the cost of ductility. The reduced ductility observed in MPEA-2 to MPEA-4 can be attributed to these factors, as Ti segregation can lead to increased strength with a ductility trade-off [71–74]. Furthermore, the reduced ductility in MPEA-2 to MPEA-4 highlights the challenges in predicting properties governed by primarily microstructural inhomogeneities.

Beyond elemental segregation, our EBSD phase maps confirm the presence of secondary phases in the Ti-enriched regions of MPEA-2 to MPEA-4, providing evidence of phase decomposition due to solute partitioning during solidification. Specifically, MPEA-2 contains ~17 % HCP phase indexed as Ti-hexagonal, while MPEA-3 and MPEA-4 each exhibit ~1 % HCP or BCC phases. These second phases form along the Ti-rich interdendritic boundaries and serve as additional barriers to dislocation motion, further enhancing local strength but also introducing elastic mismatch and phase incompatibility—both of which reduce fracture resistance. The combined presence of Ti segregation and secondary phases creates dual-mode embrittlement, offering a mechanistic explanation for the early failure observed in these alloys.

Precipitation strengthening (σ_{PPT}) is another critical factor, as solute segregation during solidification can lead to second-phase formation [71,83–85]. The presence of interdendritic Ti segregation suggests the possibility of strengthening contributions from nanoscale precipitates or solute clusters. Precipitate formation and distribution depend on processing history, which varies between alloys and is not fully captured in the ML dataset.

Twinning-induced strengthening (σ_{TW}) is another important mechanism, particularly in HEAs with low stacking fault energy, where deformation twinning contributes to strain hardening and strength enhancement [86]. Twin boundaries act as obstacles to dislocation motion, refining the effective grain size and improving mechanical properties. However, twinning activity in these alloys is not fully captured in the ML dataset, and further analysis would be needed to quantify its contribution to strengthening.

Dislocation strengthening (σ_{Dis}), also known as work hardening, depends on the dislocation density (ρ), which is influenced by prior deformation and thermal history. While this effect is significant in many alloys, the lack of direct measurements of dislocation structures in the dataset limits its consideration in ML models.

The small dataset size further limits the ML model's ability to

generalize complex relationships between composition and mechanical properties. Small datasets also increase the risk of overfitting, making ML models sensitive to noise. This issue is compounded by potential inaccuracies in literature-reported data, as discrepancies—whether due to measurement errors or inconsistencies—can introduce misleading trends in the dataset. If a significant portion of the data contains erroneous values, the ML model may struggle to establish reliable correlations, treating these incorrect data points as valid and affecting predictive accuracy.

Despite these limitations, it is important to note that ML predictions of YS and ductility for MPEA-1 aligned well with experimental results, indicating that the model can effectively identify alloys with predictable and improved properties when microstructural variability is minimal. This suggests that while current ML models may struggle with alloys that exhibit significant segregation effects or process-dependent variations, they still hold promise for guiding alloy design. The success with MPEA-1 highlights the potential of ML in discovering new alloys with optimized properties, particularly when trained on high-quality datasets with consistent microstructural information.

To further improve predictive accuracy and extend the applicability of ML models, integrating microstructural insights into the ML framework is essential. CALPHAD-based Scheil-Gulliver simulations can help model elemental partitioning, segregation tendencies and secondary phase formation during solidification, providing a more detailed understanding of composition-dependent segregation effects. Additionally, CALPHAD diffusion simulations could estimate solute redistribution and post-solidification homogenization kinetics, enabling the ML model to account for segregation-induced variations in mechanical properties. Incorporating grain size statistics, phase fractions, and segregation data into future datasets would further refine the ML approach, improving its ability to capture structure–property relationships. By leveraging these thermodynamic and kinetic modeling approaches, ML predictions can be enhanced to better reflect the interplay between solidification behavior, microstructure evolution, and mechanical performance in MPEAs.

4.2. SHAP-based feature importance in ductility predictions

While ML is helpful in the design process of complex alloys, such as MPEAs; since ML algorithms are black-box models, material scientists cannot obtain the information regarding the underlying relationships between input and target variables. But recently, Lundberg and Lee introduced Shapley additive explanations (SHAP) method to further elucidate the relationship between inputs and the target [65]. Thus, SHAP has been widely utilized by the scholars to explain ML model predictions. SHAP explains the prediction results of the model by estimating the contribution of each feature to the prediction, taking into account the calculated Shapley value, which is based on game theory. It should be noted that Shapley value can be positive or negative indicating a positive or negative impact on the target value.

The feature importance ranked by SHAP method for ductility predictions is shown in Fig. 9a, demonstrating that the annealing temperature (°C) followed by local modulus mismatch (DG), Dr, work function (WF), and bulk modulus (DelK) are the most important features with annealing temperature (°C) being on top. On Fig. 9b, the SHAP summary plot of the five most significant features is presented. It can be seen that higher values of annealing temperature (°C) resulted in a positive effect on the elongation, which can be interpreted as it caused the microstructure of the alloys to be more homogenous. On the other hand, higher values of DG showed a negative effect on the elongation based on Fig. 9b. Senkov et al. proposed an empirical model relating YS to shear modulus and shear modulus mismatch and reported that especially a higher local shear modulus mismatch among the elements contributed to an increase in the YS the most [87]. Xu et al. also highlighted that YS increases with an increasing shear modulus mismatch in their work [88]. It is a known fact for most of the alloys that an increasing YS is

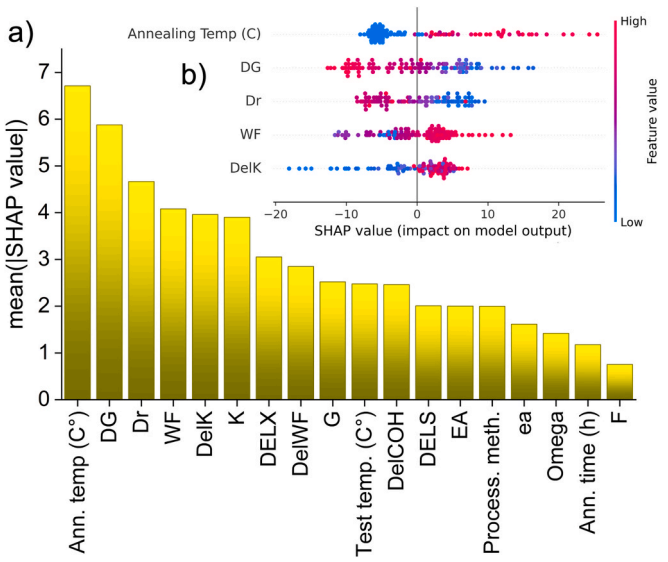


Fig. 9. SHAP analysis for ductility predictions. (a) Relative feature importance acquired by SHAP analysis for ductility predictions (since Shapley values can be negative, absolute values were used to calculate average feature importance). (b) The SHAP summary plot showing the five most important features; each datapoint denotes individual alloy data in the dataset, where the colors were assigned according to the magnitude (high or low) of the feature.

accompanied by a worsening ductility [89–91]. Hence, it can be inferred that an increasing DG would increase YS, while cause ductility to be deteriorated, as also confirmed by the SHAP analysis shown on Fig. 9b. Furthermore, the higher the Dr value is, the more negative the effect of it on the elongation as can be seen in Fig. 9b. This is consistent with the general knowledge about the effect of Dr on mechanical properties: while high atomic radii mismatch among the elements increases solid solution strengthening, excessive mismatch reduces phase stability of the solid solution and promote formation of precipitates in the microstructure, thus deteriorates the elongation [92].

The fourth important parameter, which is WF, defined as the energy required to move an electron from a bound surface state to infinity, has been shown to correlate with mechanical properties of crystalline materials, although it has been mainly used to tailor the electronic properties [93]. For instance, Hua and Li reported that WF correlates with elastic modulus of metals regardless of crystal structure [94]. It was shown that higher WF values correlate with a ductile behavior [93]. This trend was also observed for WF in our work, as demonstrated in Fig. 9b, while low and medium WF values had a negative effect of elongation. Lastly, higher values of difference in DelK have a positive effect on elongation. Since the main focus was on elongation, we report only SHAP analysis for the elongation predictions for the sake of simplicity.

5. Conclusion

In summary, we presented a machine learning (ML)-based computational framework to predict ductility yield strength (YS) of MPEAs in the CoNiVFe, CoNiVTi, CoNiVTiFe, and CoCrNiVTi alloy families, followed by experimental validation. The limitations of the use of ML method during training (due to scares data, lack of microstructural information in the research paper, and accuracy of the literature data) and the reasons for mismatch between the predictions and experimental results (especially for MPEA-2, MPEA-3, and MPEA-4) were discussed in detail. Following conclusions can be made:

1. SVR-R and RF algorithms were selected as the best algorithms to predict elongation and YS, respectively, after forward feature selection (FFS) was performed and hyperparameters were optimized.

2. The experimental elongation (78.6 ± 8.5 %) of MPEA-1 exceeded the prediction (62.3 ± 12.4 %) of SVR-R model, while experimental YS was closer to the predicted YS.
3. The experimental YS of MPEA-2 to MPEA-4 deviated from ML predictions due to the presence of Ti segregation at interdendritic regions, which was not captured in the training dataset. The localized segregation led to stress concentrations, promoting early fracture and reducing ductility beyond what was predicted.
4. The experimental results confirmed that ML models can accurately predict YS when microstructural effects such as grain boundary segregation and second-phase formation do not significantly alter mechanical properties. However, the limited dataset and absence of segregation-related features in training led to inaccuracies in predicting the ductility of MPEA-2 to MPEA-4.

These findings highlight the need for incorporating microstructural descriptors into ML frameworks to improve predictive accuracy, particularly for properties such as ductility. By integrating thermodynamic modeling and microstructural evolution data, future ML approaches can enhance their reliability, accelerating the discovery of novel high-performance alloys with tailored properties.

CRediT authorship contribution statement

H.C. Ozdemir: Writing – review & editing, Writing – original draft, Visualization, Methodology, Investigation, Formal analysis, Data curation, Conceptualization. **D. Canadinc:** Writing – review & editing, Supervision. **O. El Atwani:** Writing – review & editing, Supervision. **J. Valdez:** Writing – review & editing, Validation. **B. Lovato:** Writing – review & editing, Validation. **C. Mathews:** Writing – review & editing, Visualization, Validation. **J. Wanni:** Writing – review & editing, Visualization, Validation. **J. Cooley:** Writing – review & editing, Validation. **S.J. Fensin:** Writing – review & editing, Supervision, Project administration, Funding acquisition, Conceptualization.

Declaration of competing interest

The authors declare that they have no known competing financial interests or personal relationships that could have appeared to influence the work reported in this paper.

Acknowledgements

The authors would like to thank Derrick Williams at Los Alamos National Laboratory for performing the XRD measurements. This work was supported by the U.S. Department of Energy through the Los Alamos National Laboratory. Los Alamos National Laboratory is operated by Triad National Security, LLC, for the National Nuclear Security Administration of the U.S. Department of Energy under Contract No. 89233218CNA000001.

Appendix A. Supplementary data

Supplementary data to this article can be found online at https://doi.org/10.1016/j.matdes.2025.114434.

Data availability

All data generated or analyzed during this study are included in this published article [and its Supplementary Information Files].

The underlying code for this study is not publicly available but may be made available to qualified researchers on reasonable request from the corresponding author.

References

[1] D.B. Miracle, O.N. Senkov, A critical review of high entropy alloys and related concepts, Acta Mater. 122 (2017) 448–511, https://doi.org/10.1016/j.actamat.2016.08.081.
[2] B. Chen, L. Zhuo, Latest progress on refractory high entropy alloys: composition, fabrication, post processing, performance, simulation and prospect, Int. J. Refract. Met. Hard Mater 110 (2023) 105993, https://doi.org/10.1016/j.ijrmhm.2022.105993.
[3] O.N. Senkov, S. Gorsse, D.B. Miracle, High temperature strength of refractory complex concentrated alloys, Acta Mater. 175 (2019) 394–405, https://doi.org/10.1016/j.actamat.2019.06.032.
[4] O.N. Senkov, J.D. Miller, D.B. Miracle, C. Woodward, Accelerated exploration of multi-principal element alloys with solid solution phases, Nat. Commun. 6 (1) (2015) 1–10, https://doi.org/10.1038/ncomms7529.
[5] C.K.H. Borg, C. Frey, J. Moh, T.M. Pollock, S. Gorsse, D.B. Miracle, O.N. Senkov, B. Meredig, J.E. Saal, Expanded dataset of mechanical properties and observed phases of multi-principal element alloys, Sci. Data 7 (2020) 1–6, https://doi.org/10.1038/s41597-020-00768-9.
[6] V. Verma, C.H. Belcher, D. Apelian, E.J. Lavernia, Diffusion in high entropy alloy systems – a review, Prog. Mater. Sci. 142 (2024) 101245, https://doi.org/10.1016/j.pmatsci.2024.101245.
[7] H.C. Ozdemir, A. Nazarahari, B. Yilmaz, U. Unal, H.J. Maier, D. Canadinc, E. Bedir, R. Yilmaz, Understanding the enhanced corrosion performance of two novel Ti-based biomedical high entropy alloys, J. Alloy. Compd. 956 (2023) 170343, https://doi.org/10.1016/j.jallcom.2023.170343.
[8] Y. Shi, B. Yang, X. Xie, J. Brechtl, K.A. Dahmen, P.K. Liaw, Corrosion of Al xCoCrFeNi high-entropy alloys: Al-content and potential scan-rate dependent pitting behavior, Corros. Sci. 119 (2017) 33–45, https://doi.org/10.1016/j.corsci.2017.02.019.
[9] Y. Zhao, M. Wang, H. Cui, Y. Zhao, X. Song, Y. Zeng, X. Gao, F. Lu, C. Wang, Q. Song, Effects of Ti-to-Al ratios on the phases, microstructures, mechanical properties, and corrosion resistance of Al2-xCoCrFeNiTix high-entropy alloys, J. Alloy. Compd. 805 (2019) 585–596, https://doi.org/10.1016/j.jallcom.2019.07.100.
[10] Z.Q. Xu, Z.L. Ma, Y. Tan, M. Wang, Y. Zhao, X.W. Cheng, Effects of Si additions on microstructures and mechanical properties of VNbTiTaSix refractory high-entropy alloys, J. Alloy. Compd. 900 (2022) 163517, https://doi.org/10.1016/j.jallcom.2021.163517.
[11] N.D. Stepanov, D.G. Shaysultanov, M.A. Tikhonovsky, G.A. Salishchev, Tensile properties of the Cr-Fe-Ni-Mn non-equiatomic multicomponent alloys with different Cr contents, Mater. Des. 87 (2015) 60–65, https://doi.org/10.1016/j.matdes.2015.08.007.
[12] J.W. Bae, J.B. Seol, J. Moon, S.S. Sohn, M.J. Jang, H.Y. Um, B.J. Lee, H.S. Kim, Exceptional phase-transformation strengthening of ferrous medium-entropy alloys at cryogenic temperatures, Acta Mater. 161 (2018) 388–399, https://doi.org/10.1016/J.ACTAMAT.2018.09.057.
[13] B. Schuh, B. Völker, J. Todt, N. Schell, L. Perrière, J. Li, J.P. Couzinié, A. Hohenwarter, Thermodynamic instability of a nanocrystalline, single-phase TiZrNbHfTa alloy and its impact on the mechanical properties, Acta Mater. 142 (2018) 201–212, https://doi.org/10.1016/j.actamat.2017.09.035.
[14] Q. Wang, Y. Ma, B. Jiang, X. Li, Y. Shi, C. Dong, P.K. Liaw, A cuboidal B2 nanoprecipitation-enhanced body-centered-cubic alloy Al0.7CoCrFe2Ni with prominent tensile properties, Scripta Materialia 120 (2016) 85–89, https://doi.org/10.1016/j.scriptamat.2016.04.014.
[15] B. Cantor, I.T.H. Chang, P. Knight, A.J.B. Vincent, Microstructural development in equiatomic multicomponent alloys, Mater. Sci. Eng. A 375–377 (2004) 213–218, https://doi.org/10.1016/j.msea.2003.10.257.
[16] F. Otto, A. Dlouhý, C. Somsen, H. Bei, G. Eggeler, E.P. George, The influences of temperature and microstructure on the tensile properties of a CoCrFeMnNi high-entropy alloy, Acta Mater. 61 (2013) 5743–5755, https://doi.org/10.1016/J.ACTAMAT.2013.06.018.
[17] O.N. Senkov, G.B. Wilks, J.M. Scott, D.B. Miracle, Mechanical properties of Nb25Mo25Ta 25W25 and V20Nb20Mo 20Ta20W20 refractory high entropy alloys, Intermetallics 19 (2011) 698–706, https://doi.org/10.1016/j.intermet.2011.01.004.
[18] E.P. George, W.A. Curtin, C.C. Tasan, High entropy alloys: a focused review of mechanical properties and deformation mechanisms, Acta Mater. 188 (2020) 435–474, https://doi.org/10.1016/j.actamat.2019.12.015.
[19] W. Xiong, A.X.Y. Guo, S. Zhan, C.T. Liu, S.C. Cao, Refractory high-entropy alloys: a focused review of preparation methods and properties, J. Mater. Sci. Technol. 142 (2023) 196–215, https://doi.org/10.1016/j.jmst.2022.08.046.
[20] G. Chen, H. Yan, Z. Wang, K. Wang, N.I. Yves, Y. Tong, Effects of Mo content on the microstructure and mechanical properties of TiNbZrMox high-entropy alloys, J. Alloy. Compd. 930 (2023) 167373, https://doi.org/10.1016/j.jallcom.2022.167373.
[21] S. Sheikh, S. Shafeie, Q. Hu, J. Ahlström, C. Persson, J. Veselý, J. Zýka, U. Klement, S. Guo, Alloy design for intrinsically ductile refractory high-entropy alloys, J. Appl. Phys. 120 (2016) 164902, https://doi.org/10.1063/1.4966659.
[22] C. Zhu, X. Li, Z. Zhang, Phase evolution and mechanical properties of Ti1.5NbVAlx (x=0.25, 0.5, 0.75, 1) lightweight refractory medium-entropy alloys, Vacuum 221 (2024) 112888, https://doi.org/10.1016/j.vacuum.2023.112888.
[23] Y. Fu, J. Li, H. Luo, C. Du, X. Li, Recent advances on environmental corrosion behavior and mechanism of high-entropy alloys, J. Mater. Sci. Technol. 80 (2021) 217–233, https://doi.org/10.1016/j.jmst.2020.11.044.

[24] L. Qiao, Y. Liu, J. Zhu, A focused review on machine learning aided high-throughput methods in high entropy alloy, J. Alloy. Compd. 877 (2021) 160295, https://doi.org/10.1016/j.jallcom.2021.160295.
[25] S. Singh, N.K. Katiyar, S. Goel, S.N. Joshi, Phase prediction and experimental realisation of a new high entropy alloy using machine learning, Sci. Rep. 13 (2023) 4811, https://doi.org/10.1038/s41598-023-31461-7.
[26] X. Liu, J. Zhang, Z. Pei, Machine learning for high-entropy alloys: progress, challenges and opportunities, Prog. Mater Sci. 131 (2022) 101018, https://doi.org/10.1016/J.PMATSCI.2022.101018.
[27] T.C. Nguyen, Y.S. So, J.S. Yoo, J.G. Kim, Machine learning modeling of predictive external corrosion rates of spent nuclear fuel carbon steel canister in soil, Sci. Rep. 12 (1) (2022) 1–17, https://doi.org/10.1038/s41598-022-24783-5.
[28] H.C. Ozdemir, A. Nazarahari, B. Yilmaz, D. Canadinc, E. Bedir, R. Yilmaz, U. Unal, H.J. Maier, Machine learning – informed development of high entropy alloys with enhanced corrosion resistance, Electrochim. Acta 476 (2024) 143722, https://doi.org/10.1016/j.electacta.2023.143722.
[29] N.J. Sai, P. Rathore, A. Chauhan, Machine learning-based predictions of fatigue life for multi-principal element alloys, Scr. Mater. 226 (2023) 115214, https://doi.org/10.1016/j.scriptamat.2022.115214.
[30] H.C. Ozdemir, E. Bedir, R. Yilmaz, M.B. Yagci, D. Canadinc, Machine learning-assisted design of biomedical high entropy alloys with low elastic modulus for orthopedic implants, J. Mater. Sci. 57 (2022) 11151–11169, https://doi.org/10.1007/s10853-022-07363-w.
[31] H. Khakurel, M.F.N. Taufique, A. Roy, G. Balasubramanian, G. Ouyang, J. Cui, D. D. Johnson, R. Devanathan, Machine learning assisted prediction of the Young's modulus of compositionally complex alloys, Sci. Rep. 11 (2021) 1–10, https://doi.org/10.1038/s41598-021-96507-0.
[32] H. Chang, Y. Tao, P.K. Liaw, J. Ren, Phase prediction and effect of intrinsic residual strain on phase stability in high-entropy alloys with machine learning, J. Alloy. Compd. 921 (2022) 166149, https://doi.org/10.1016/j.jallcom.2022.166149.
[33] K. Lee, M.V. Ayyasamy, P. Delsa, T.Q. Hartnett, P.V. Balachandran, Phase classification of multi-principal element alloys via interpretable machine learning, NPJ Comput. Mater. 8 (2022) 1–12, https://doi.org/10.1038/s41524-022-00704-y.
[34] W. Huang, P. Martin, H.L. Zhuang, Machine-learning phase prediction of high-entropy alloys, Acta Mater. 169 (2019) 225–236, https://doi.org/10.1016/j.actamat.2019.03.012.
[35] Y.F. Zhang, W. Ren, W.L. Wang, N. Li, Y.X. Zhang, X.M. Li, W.H. Li, Interpretable hardness prediction of high-entropy alloys through ensemble learning, J. Alloy. Compd. 945 (2023) 169329, https://doi.org/10.1016/j.jallcom.2023.169329.
[36] A.A. Catal, E. Bedir, R. Yilmaz, M.A. Swider, C. Lee, O. El-Atwani, H.J. Maier, H. C. Ozdemir, D. Canadinc, Machine learning assisted design of novel refractory high entropy alloys with enhanced mechanical properties, Comput. Mater. Sci. 231 (2024) 112612, https://doi.org/10.1016/j.commatsci.2023.112612.
[37] U. Bhandari, M.R. Rafi, C. Zhang, S. Yang, Yield strength prediction of high-entropy alloys using machine learning, Mater. Today Commun. 26 (2021) 101871, https://doi.org/10.1016/j.mtcomm.2020.101871.
[38] M.R. Zamani, M. Roostaei, H. Mirzadeh, M. Malekan, M. Song, Tailoring the microstructure and mechanical properties of (CrMnFeCoNi)100-xCx high-entropy alloys: machine learning, experimental validation, and mathematical modeling, Curr. Opin. Solid State Mater. Sci. 27 (2023) 101105, https://doi.org/10.1016/j.cossms.2023.101105.
[39] K. Xu, J. An, L. Zhang, C. Bai, J. Tu, J. Luo, Composition optimization of cobalt-free Fe-Cr-Ni-Al/Ti multi-principal element alloys for strength-ductility trade-off based on machine learning, Mater. Today Commun. 36 (2023) 106498, https://doi.org/10.1016/J.MTCOMM.2023.106498.
[40] M. Veeresham, S. Narayanaswamy, M. Kang, S.W. Joo, U. Lee, N. Park, Utilizing an intelligent machine learning strategy for predicting the tensile strength and ductility properties of nitrogen doped CoCrFeMnNi based high entropy alloys, J. Alloy. Compd. 976 (2024) 173089, https://doi.org/10.1016/J.JALLCOM.2023.173089.
[41] X. Zhao, Z. Wei, J. Zhao, Y. Jia, S. Cao, D. Wang, Y. Lei, Machine-learning-assisted design of novel TiZrNbVAl refractory high-entropy alloys with enhanced ductility, Metals 14 (2024) 894, https://doi.org/10.3390/MET14080894.
[42] Z. Li, S. Li, N. Birbilis, A machine learning-driven framework for the property prediction and generative design of multiple principal element alloys, Mater. Today Commun. 38 (2024) 107940, https://doi.org/10.1016/J.MTCOMM.2023.107940.
[43] E. Gerashi, M. Pourbaghi, X. Duan, A. Zavdoveev, A. Klapatyuk, J. Shen, A. Hatefi, S.A. Alidokht, Machine learning-aided phase and mechanical properties prediction in multi-principal element alloys, Comput. Mater. Sci. 243 (2024) 113114, https://doi.org/10.1016/J.COMMATSCI.2024.113114.
[44] Z. Jiang, W. Chen, C. Chu, Z. Fu, Y. Lu, Y. Ivanisenko, Lamellar-structured low-cost FeMn0.7Ni0.6Cr0.4Al0.3 high entropy alloy with excellent tensile properties, Vacuum 209 (2023) 111767, https://doi.org/10.1016/J.VACUUM.2022.111767.
[45] Z. Tian, T. Zhang, Z. Wang, Z. Xie, F. Fang, Dynamic tensile deformation of Al0.1Ti0.1CoCrFeNi high entropy alloy with heterogeneous grain structure, J. Alloys Compd. 968 (2023) 172092, https://doi.org/10.1016/J.JALLCOM.2023.172092.
[46] S.H. Shim, H. Pouraliakbar, S.I. Hong, Hierarchical structured as-cast CrFeNiMn0.5Cu0.5 high entropy alloy with excellent tensile strength/ductility properties, Scripta Materialia 210 (2022) 114473, https://doi.org/10.1016/J.SCRIPTAMAT.2021.114473.
[47] J. Wang, Q. Wu, Y. Li, Z. Wang, J. Li, J. Wang, Phase selection of BCC/B2 phases for the improvement of tensile behaviors in FeNiCrAl medium entropy alloy, J. Alloy. Compd. 916 (2022) 165382, https://doi.org/10.1016/J.JALLCOM.2022.165382.
[48] Z. Cai, N. Wei, Y. Han, F. Si, L. Mi, C. Zhang, X. Liu, F. Jiang, T. Wu, Effect of heat treatment on microstructure, tensile properties and high-temperature corrosion resistance of the FeCrMnNi high entropy alloy, Metals 12 (2022) 1537, https://doi.org/10.3390/MET12091537.
[49] H. Jiang, D. Qiao, W. Jiao, K. Han, L. Yiping, P.K. Liaw, Tensile deformation behavior and mechanical properties of a bulk cast Al0.9CoFeNi2 eutectic high-entropy alloy, J. Mater. Sci. Technol. 61 (2021) 119–124, https://doi.org/10.1016/J.JMST.2020.05.053.
[50] D. Li, Y. Dong, Z. Zhang, Q. Zhang, S. Chen, N. Jia, H. Wang, B. Wang, K. Jin, Y. Xue, Y. Dou, X. He, W. Yang, L. Wang, H. Cai, An as-cast Ti-V-Cr-Al light-weight medium entropy alloy with outstanding tensile properties, J. Alloy. Compd. 877 (2021) 160199, https://doi.org/10.1016/J.JALLCOM.2021.160199.
[51] Q. Wang, L. Zeng, T. Gao, H. Du, X. Liu, On the room-temperature tensile deformation behavior of a cast dual-phase high-entropy alloy CrFeCoNiAl0.7, J. Mater. Sci. Technol. 87 (2021) 29–38, https://doi.org/10.1016/J.JMST.2021.01.053.
[52] J. Zhou, H. Liao, H. Chen, A. Huang, Microstructure and tensile mechanical behavior of a single-phase Fe35Mn10Cr20Ni35 high-entropy alloy, J. Mater. Eng. Perform. 30 (2021) 3352–3362, https://doi.org/10.1007/S11665-021-05700-9/METRICS.
[53] J. Niu, Z. Fu, W. Chen, T. Lu, L. Hao, W. Xiong, H. Wen, Hierarchical microstructure enables high strength and good ductility in as-cast Fe27Ni35Cr18.25Al13.75Co2Ti2Mo2 high-entropy alloy, J. Mater. Sci. Technol. 179 (2024) 9–21, https://doi.org/10.1016/J.JMST.2023.08.054.
[54] W. Wu, H. Fu, Z. Xue, W. Fan, B. Gan, N. Jiang, M. Xia, F. Zhao, Synergistic effect of Al and Ti micro-alloying in CoCrNi-based medium entropy alloy, J. Mater. Res. Technol. 29 (2024) 1962–1970, https://doi.org/10.1016/J.JMRT.2024.01.118.
[55] T.J. Song, S.B. Jin, J.A. Chen, M.Y. Yu, J.M. Zhu, The influences of vanadium addition and temperature on the microstructure, and mechanical properties of Al0.1CoCrFeNiVx multi-principal element alloys, J. Alloys Compd. 979 (2024) 173581, https://doi.org/10.1016/J.JALLCOM.2024.173581.
[56] C. Wen, Y. Zhang, C. Wang, D. Xue, Y. Bai, S. Antonov, L. Dai, T. Lookman, Y. Su, Machine learning assisted design of high entropy alloys with desired property, Acta Mater. 170 (2019) 109–117, https://doi.org/10.1016/j.actamat.2019.03.010.
[57] S. Guo, Phase selection rules for cast high entropy alloys: an overview, Mater. Sci. Technol. (United Kingdom) 31 (2015) 1223–1230, https://doi.org/10.1179/1743284715Y.0000000018.
[58] A.K. Singh, N. Kumar, A. Dwivedi, A. Subramaniam, A geometrical parameter for the formation of disordered solid solutions in multi-component alloys, Intermetallics 53 (2014) 112–119, https://doi.org/10.1016/j.intermet.2014.04.019.
[59] Z. Wang, Y. Huang, Y. Yang, J. Wang, C.T. Liu, Atomic-size effect and solid solubility of multicomponent alloys, Scr. Mater. 94 (2015) 28–31, https://doi.org/10.1016/j.scriptamat.2014.09.010.
[60] I. Toda-Caraballo, P.E.J. Rivera-Díaz-Del-Castillo, Modelling solid solution hardening in high entropy alloys, Acta Mater. 85 (2015) 14–23, https://doi.org/10.1016/J.ACTAMAT.2014.11.014.
[61] C. Varvenne, A. Luque, W.A. Curtin, Theory of strengthening in fcc high entropy alloys, Acta Mater. 118 (2016) 164–176, https://doi.org/10.1016/J.ACTAMAT.2016.07.040.
[62] A. Katrutsa, V. Strijov, Comprehensive study of feature selection methods to solve multicollinearity problem according to evaluation criteria, Expert Syst. Appl. 76 (2017) 1–11, https://doi.org/10.1016/j.eswa.2017.01.048.
[63] J. Huang, W. Fang, C. Xue, T. Peng, H. Yu, J. Li, L. Sun, X. He, B. Liu, Y. Yang, F. Yin, Exploring the relationship between lattice distortion and phase stability in a multi-principal element alloy system based on machine learning method, Comput. Mater. Sci. 221 (2023) 112089, https://doi.org/10.1016/j.commatsci.2023.112089.
[64] L. Chen, A. Jarlöv, H.L. Seet, M.L.S. Nai, Y. Li, K. Zhou, Exploration of V–Cr–Fe–Co–Ni high-entropy alloys with high yield strength: a combination of machine learning and molecular dynamics simulation, Comput. Mater. Sci. 217 (2023) 111888, https://doi.org/10.1016/j.commatsci.2022.111888.
[65] S.M. Lundberg, S.I. Lee, A unified approach to interpreting model predictions, in: Advances in Neural Information Processing Systems, 2017: pp. 4766–4775. https://doi.org/10.5555/3295222.
[66] X. Liu, P. Xu, J. Zhao, W. Lu, M. Li, G. Wang, Material machine learning for alloys: applications, challenges and perspectives, J. Alloy. Compd. 921 (2022) 165984, https://doi.org/10.1016/j.jallcom.2022.165984.
[67] Z. He, L. Li, Z. Huang, H. Situ, Quantum-enhanced feature selection with forward selection and backward elimination, Quantum Inf. Process 17 (2018) 1–11, https://doi.org/10.1007/s11128-018-1924-8.
[68] A. Roy, M.F.N. Taufique, H. Khakurel, R. Devanathan, D.D. Johnson, G. Balasubramanian, Machine-learning-guided descriptor selection for predicting corrosion resistance in multi-principal element alloys, NPJ Mater. Degrad. 6 (2022) 1–10, https://doi.org/10.1038/s41529-021-00208-y.
[69] W. Kurz, D.J. Fisher, M. Rappaz, Fundamentals of Solidification 5th Fully Revised Edition, Trans Tech Publications Ltd, 2023. https://doi.org/10.4028/b-v7b35q.
[70] L. Jiang, Y.P. Lu, M. Song, C. Lu, K. Sun, Z.Q. Cao, T.M. Wang, F. Gao, L.M. Wang, A promising CoFeNi2V0.5Mo0.2 high entropy alloy with exceptional ductility, Scripta Materialia 165 (2019) 128–133, https://doi.org/10.1016/J.SCRIPTAMAT.2019.02.038.
[71] T.R. Smith, J.D. Sugar, C. San Marchi, J.M. Schoenung, Strengthening mechanisms in directed energy deposited austenitic stainless steel, Acta Materialia 164 (2019) 728–740, https://doi.org/10.1016/j.actamat.2018.11.021.

[72] J. Wanni, A. Achuthan, Hetero-deformation induced (HDI) strengthening in directed energy deposited SS316L: a nanoindentation-based investigation, Mater. Sci. Eng. A 860 (2022) 144280, https://doi.org/10.1016/j.msea.2022.144280.
[73] L. Liu, Q. Ding, Y. Zhong, J. Zou, J. Wu, Y.-L. Chiu, J. Li, Z. Zhang, Q. Yu, Z. Shen, Dislocation network in additive manufactured steel breaks strength–ductility trade-off, Mater. Today 21 (2018) 354–361, https://doi.org/10.1016/j.mattod.2017.11.004.
[74] I. Basu, J.T.M. De Hosson, Strengthening mechanisms in high entropy alloys: fundamental issues, Scr. Mater. 187 (2020) 148–156, https://doi.org/10.1016/j.scriptamat.2020.06.019.
[75] H. Li, J. Wang, W. Zhang, J. Zhao, J. Li, M.W. Fu, Achieving superior ductility with ultrahigh strength via deformation and strain hardening in the non-recrystallized regions of the heterogeneous-structured high-entropy alloy, Acta Mater. 283 (2025) 120572, https://doi.org/10.1016/j.actamat.2024.120572.
[76] K. Ma, H. Wen, T. Hu, T.D. Topping, D. Isheim, D.N. Seidman, E.J. Lavernia, J. M. Schoenung, Mechanical behavior and strengthening mechanisms in ultrafine grain precipitation-strengthened aluminum alloy, Acta Mater. 62 (2014) 141–155, https://doi.org/10.1016/j.actamat.2013.09.042.
[77] D. Wu, J. Zhang, J.C. Huang, H. Bei, T.G. Nieh, Grain-boundary strengthening in nanocrystalline chromium and the Hall–Petch coefficient of body-centered cubic metals, Scr. Mater. 68 (2013) 118–121, https://doi.org/10.1016/j.scriptamat.2012.09.025.
[78] Effect of Interstitial Elements on Hall–Petch Coefficient of Ferritic Iron, (n.d.). https://www.jstage.jst.go.jp/article/isijinternational/48/8/48_8_1122/_article (accessed June 11, 2025).
[79] B. Gwalani, V. Soni, M. Lee, S. Mantri, Y. Ren, R. Banerjee, Optimizing the coupled effects of Hall-Petch and precipitation strengthening in a Al0.3CoCrFeNi high entropy alloy, Mater. Des. 121 (2017) 254–260, https://doi.org/10.1016/j.matdes.2017.02.072.
[80] S.N. Naik, S.M. Walley, The Hall–Petch and inverse Hall–Petch relations and the hardness of nanocrystalline metals, J. Mater. Sci. 55 (2020) 2661–2681, https://doi.org/10.1007/s10853-019-04160-w.
[81] H.A. Roth, C.L. Davis, R.C. Thomson, Modeling solid solution strengthening in nickel alloys, Metall. Mater. Trans. A 28 (1997) 1329–1335, https://doi.org/10.1007/s11661-997-0268-2.
[82] J. Freudenberger, F. Thiel, D. Utt, K. Albe, A. Kauffmann, S. Seils, M. Heilmaier, Solid solution strengthening in medium- to high-entropy alloys, Mater. Sci. Eng. A 861 (2022) 144271, https://doi.org/10.1016/j.msea.2022.144271.
[83] W.H. Liu, T. Yang, C.T. Liu, Precipitation hardening in CoCrFeNi-based high entropy alloys, Mater. Chem. Phys. 210 (2018) 2–11, https://doi.org/10.1016/j.matchemphys.2017.07.037.
[84] L. Zhang, X. Huo, A. Wang, X. Du, L. Zhang, W. Li, N. Zou, G. Wan, G. Duan, B. Wu, A ductile high entropy alloy strengthened by nano sigma phase, Intermetallics 122 (2020) 106813, https://doi.org/10.1016/J.INTERMET.2020.106813.
[85] F. He, D. Chen, B. Han, Q. Wu, Z. Wang, S. Wei, D. Wei, J. Wang, C.T. Liu, J. Kai, Design of D022 superlattice with superior strengthening effect in high entropy alloys, Acta Materialia 167 (2019) 275–286, https://doi.org/10.1016/J.ACTAMAT.2019.01.048.
[86] Z. Li, K.G. Pradeep, Y. Deng, D. Raabe, C.C. Tasan, Metastable high-entropy dual-phase alloys overcome the strength–ductility trade-off, Nature 534 (2016) 227–230, https://doi.org/10.1038/nature17981.
[87] O.N. Senkov, J.M. Scott, S.V. Senkova, D.B. Miracle, C.F. Woodward, Microstructure and room temperature properties of a high-entropy TaNbHfZrTi alloy, J. Alloy. Compd. 509 (2011) 6043–6048, https://doi.org/10.1016/j.jallcom.2011.02.171.
[88] Z. Xu, B. Wu, G. Wan, L. Zhang, X. Du, Y. Liu, C. Esling, Evolution of tensile strength and ductility of the non-equimolar TiVNbMoCr alloys with maximum entropy under the VEC constraint, Mater. Sci. Eng. A 901 (2024) 146514, https://doi.org/10.1016/J.MSEA.2024.146514.
[89] S.X. Liang, M.Z. Ma, R. Jing, Y.K. Zhou, Q. Jing, R.P. Liu, Preparation of the ZrTiAlV alloy with ultra-high strength and good ductility, Mater. Sci. Eng. A 539 (2012) 42–47, https://doi.org/10.1016/J.MSEA.2012.01.022.
[90] R. Fan, L. Wang, L. Zhao, L. Wang, S. Zhao, Y. Zhang, B. Cui, Synergistic effect of Nb and Mo alloying on the microstructure and mechanical properties of CoCrFeNi high entropy alloy, Mater. Sci. Eng. A 829 (2022) 142153, https://doi.org/10.1016/J.MSEA.2021.142153.
[91] Q. Liu, G. Wang, X. Sui, Y. Xu, Y. Liu, J. Yang, Ultra-fine grain TixVNbMoTa refractory high-entropy alloys with superior mechanical properties fabricated by powder metallurgy, J. Alloy. Compd. 865 (2021) 158592, https://doi.org/10.1016/j.jallcom.2020.158592.
[92] B. Dou, J. Cui, R. Guo, S. Liu, T. Zhang, S. Chen, B. Li, X. Wang, B. Wang, S. Sun, L. Wang, Y. Xue, Modulus-mismatch strategy optimized lightweight refractory high-entropy alloys for superior synergy of mechanical properties and thermostability, Mater. Sci. Eng. A 908 (2024) 146767, https://doi.org/10.1016/J.MSEA.2024.146767.
[93] X.F. Wang, T.E. Jones, Y. Wu, Z.P. Lu, S. Halas, T. Durakiewicz, M.E. Eberhart, An electronic criterion for assessing intrinsic brittleness of metallic glasses, J. Chem. Phys. 141 (2014) 52, https://doi.org/10.1063/1.4884783/352364.
[94] G. Hua, D. Li, Generic relation between the electron work function and Young's modulus of metals, Appl. Phys. Lett. 99 (2011) 041907, https://doi.org/10.1063/1.3614475.